Geologic Carbon Storage: Implications of Two-Phase Flow on Injection-Induced Stress on Faults

Samir Prasun[1], Seunghee Kim[2], Seyyed A. Hosseini[3]
1. Petroleum Engineering, Louisiana State University, Baton Rouge, LA, USA
2. Department of Civil Engineering, University of Nebraska-Lincoln, Omaha, NE, USA
3. Bureau of Economic Geology, Jackson School of Geosciences, University of Texas at Austin, Austin, TX, USA
*Corresponding author: Office 3218, 3304 Patrick F Taylor hall, Baton Rouge, LA 70803, USA,
prasoonsamir@gmail.com

Abstract

Geologic carbon storage that involves injecting carbon dioxide (CO_2) into a subsurface sequestration site provides the vital approach for reducing CO_2 emissions into atmosphere and thus addressing climate change issue. One challenge associated with CO_2 geologic storage is that pore-pressure buildup and subsequent poroelastic stress changes during CO_2 injection may result in injection-induced seismicity on faults. Most of previous studies implemented numerical simulations based on a single-phase fluid flow condition during CO_2 injection into a saline aquifer to investigate such a concern. This preposition neglects the effect of high compressibility of CO_2 and low hydraulic diffusivity of two phase flow system, which may lead to an incorrect estimate of the poroelastic stress changes on faults.

The simulation method in this study employs the Equation Based Modeling interface (i.e., coefficient form PDE module) in COMSOL to solve non-linear partial differential equations (PDE) with two dependent variables, 'saturation' and 'fluid-phase pressure' that define the two-phase CO_2 and water immiscible flow. The equations include the gravity, capillary and fluid compressibility effects. The effect of solid deformation on pore pressure in the source term defines the solid-to-fluid coupling. The relative permeability interpolation table defines the mobility of each phase in a saline formation. The fluid-to-solid coupling is introduced by coupling PDE module with the COMSOL solid-mechanics interface that governs the change of stresses as a function of pressure. During the simulation, a constant injection rate of CO_2 is imposed on the sandstone formation that is underlain by the basement rock with faults in it and overlain by an impermeable mudrock.

Inclusion of two-phase flow condition results in the high pressure buildup near the CO_2 injection source due to lower hydraulic diffusivity, which causes slower pore pressure diffusion and hence higher pore pressure buildup in the injection aquifer close to the injection. As a result, the single-phase flow assumption significantly underestimates the pore pressure build up and the coulomb stress changes in the target formation and faults in the basement where direct pore pressure changes occur. This implies that the single-phase flow assumption can substantially underestimate the likelihood of injection-induced seismicity, particularly in conductive faults that are connected to the target formation. Further, both single and multiphase fluid flow simulation demonstrated the larger change in the coulomb stress on faults where direct diffusion of pore pressure occurs, compared to the case where indirect poroelastic effect induces smaller changes in the coulomb stress on faults.

Keywords: CO_2 geologic storage, COMSOL, two-phase flow, poroelastic stress, faults

1. Introduction

Carbon capture, utilization and storage involves transporting carbon dioxide (CO_2), which is captured from the emission source, and injecting into the subsurface sequestration site. One of the major challenges that includes managing pore-pressure build up during carbon dioxide injection and thereby further ensuring mechanical integrity remains to be addressed for the successful operation of geologic carbon dioxide storage. Important question is how to maximize the CO_2 injection without causing any mechanical failure. This drives us to investigate the poroelastic effect of pore pressure buildup on the stress-field pattern during CO_2 injection, which will enable us to optimize the injection rate, pressure and volume.

Over the past years, the central and eastern United States has experienced high levels of seismic activities near sites of deep injection of wastewater (Horton 2012; Kim 2013; Ellsworth 2013; Kerenan et al.

2013). The importance of geomechanics has recently become more widely recognized as the possible consequences of the large-scale geologic CO_2 storage operations (Zoback 2010). There are concerns related to the potential for triggering seismic events and how such events could impact the long-term integrity of a CO_2 storage (Zoback 2010). For instance, microseismicity ($\leq$ magnitude 2.0) was observed during CO_2 capture and storage project in the Illinois Basin-Decatur Project (Bauer et al. 2016). Shut-down of a geothermal project in Basel after a 3.4 magnitude of seismic event (Häring et al. 2008) is a well-known example. Another example is the In Salah CO_2 storage project where significant geomechanical changes have been observed. All this necessitates the thorough understanding of geomechanical impact of CO_2 injection-induced overpressure which may potentially trigger the injection-induced seismicity in the underlying basement rock of CO_2 injection zone, especially along the faults or fractures within them.

Above discussion demands the accurate prediction of injection-induced pore pressure build up and the resulting poroelastic stress changes due to CO_2 sequestration. However, in the past, simplified models were used for studying large-scale geomechanical impacts of the CO_2 storage and assessing the potential for fault reactivation, driven by large-scale reservoir pressure changes (e.g. Chiaramonte et al. 2011). For example, traditional approaches (Hillis 2000; 2001; Kim and Hosseini 2013; 2014; 2015; 2017) employed the single-phase flow condition in a saline aquifer, and hence ignored the effect of CO_2 compressibility in slowing or accelerating the diffusion and dissipation of injection induced overpressure. The single-phase flow assumption may incorrectly estimate the pore pressure changes which may result in an inaccurate estimate of the poroelastic stress changes both due to direct diffusion of pore pressure or indirect transfer from change in pore pressure. This may potentially lead to inaccurate prediction of the injection-induced seismicity.

Apparently, several studies considered the effects of multiphase flow (including capillary effects) and partial or full coupling between pore pressure and deformation of solids in the multi-phase poro-mechanical simulators to study the geomechanical impact of CO_2 injection. These include simulation works using TOUGH-FLAC (Rutqvist et al. 2002; Rutqvist 2011) that sequentially couples the fluid-flow and geomechanics; FEMH (Bower and Zyvoloski 1997; Deng et al. 2011) that incorporates the fully implicit but sequentially coupled approach to solve poro-mechanical fluid-flow equation in dual porosity fractured media; CODE-BRIGHT (Olivella et al. 1994; Vilarrasaa et al. 2010) that uses finite element in space and finite difference in time for discretization of governing partial differential equations; ECLIPSE-VISAGE (Ouellet et al. 2011) that utilizes a one-way partial coupling method to combine finite difference fluid-flow simulator ECLIPSE and finite element mechanical simulator VISAGE; STARS (CMG 2003; Bissell et al. 2011) that uses finite difference approach for multi-phase flow simulation; DYNAFLOW (Preisig and Prévost 2011) that incorporates the finite difference and fully coupled approach to include the effect of deformation on fluid-flow; GPAS (Pan et al. 2007) that is a finite element compositional and explicitly coupled poro-mechanical simulator; UTCOMP (Haddad and Sepehnoori 2009) that is explicitly coupled with geomechanics using Chin's iteratively coupled method (Chin et al. 2002); as well as other simulators in which multiphase flow codes such as TOUGH2, ECLIPSE, and GEM have been linked with geomechanical codes (e.g. Rohmer and Seyedi 2010; Ferronato et al. 2010). Moreover, these numerical multiphase flow models have also been lined with analytical geomechanical models (e.g. Lucier et al. 2006; Chiaramonte et al. 2008; Vidal-Gilbert et al. 2010). Though these numerical schemes paved the path for multi-phase poro-mechanical simulation, most of them suffer from drawbacks that include: 1) use of finite difference method as the discretization scheme, 2) use of IMPES or IMPEC method in solving governing partial differential equation that requires small time-step, 3) use of partial coupling (example explicit or iterative coupling in which geomechanics module is solved separately (or iteratively) after solving for the reservoir pressure and the new porosity and permeability value is updated in the next time-step) may differ significantly from the predictions of full coupling; 4) consisting of linear solver which is not able to solve discretized non-linear equations, and lastly 5) requirement of programming meshes for uniform domains that disregards their adoption for any non-uniform formation geometries like slanted faults or anticlinal structure. On the other hand, COMSOL 'Poroelasticity' model utilizes a fully implicit and fully coupled approach to solve geomechanics and fluid-flow equations together. It is capable of solving non-linear discretized equations using Newton-Rhapson iteration scheme (COMSOL 2015).

COMSOL also has an automatic meshing system, so one does not need to program the mesh. In addition, there are ways to refine the mesh in some regions or at some boundaries. Those features make it very convenient to investigate engineering problems with a complex domain and many internal boundaries, especially in three dimension (3D).

There are few researchers (Pan et al. 2007; Haddad and Sepehrnoor 2009) in the past who incorporated the porosity term into the explicit coupling equations between the fluid flow and geomechanics to account for the effect of deformation on the change in true porosity. This study follows the fully-coupled approach of Jaeger et al. 2007; Chang and Segall 2016; and Kim and Hosseini 2017, which introduced the effect of deformation on each phase as a separate source term to each phase's governing partial differential equation.

Goal of this study is to examine the effect of multiphase flow and CO_2 compressibility on the injection induced stress changes for conductive basement faults connected to the target storage formation. The simulation work was performed using COMSOL Multiphysics software that solves differential equations for any complicated structure based on finite element method. This study aims to compare results from the two-phase (CO_2+water) fluid flow conditions with those from the single-phase flow condition to justify the need to employ the two-phase numerical model.

2. Model Problem

Poroelasticity involves coupling solid deformation with the pore pressure diffusion. In this study, the model consists of permeable aquifer injection layer surrounded by the top and bottom impermeable layers such that their mechanical and hydrological properties differ from each other. Major assumptions to derive the two phase (CO_2 and water) governing equations of poroelasticity during geologic CO_2 injection process are: 1) medium is linear, isotropic and elastic, 2) isothermal condition prevails, 3) supercritical CO_2 diffusion and dissolution in the saline aquifer is ignored, 4) both CO_2 and water flow follows Darcy's law. In this study, we perform full coupling in which displacement and stresses are computed based on the pore pressure build-up, and vice-versa, so both stresses and pore pressure are solved simultaneously.

For simulating the single-phase fluid (water) flow process during water injection and two-phase fluid flow process during CO_2 injection, commercial software COMSOL Multiphysics is used to generate the stress and pore pressure fields in the formation. The built-in subsurface module in COMSOL does not account for the compressibility of fluids along with the poroelasticity (geomechanics) effects. So, we used the equation based modeling interface in COMSOL in which various types of partial differential equation (PDEs) can be solved using different formulations.

2.1 Governing Equations for Single Phase Flow

In this formulation, we will combine the constitutive equation of solid mechanics with the transient formulations of single-phase fluid flow based on Biot's theory (COSMOL 2015; Kim and Hosseini 2017; Jaeger et al. 2007). The constitutive equation that relates stress and strain is given by,

$$\sigma = C\varepsilon - \alpha p_f I \tag{1}$$

Where, elasticity matrix C in Eq. (1) must be measured under drained condition, I is an identity matrix, and p_f is the pore-pressure. From the mass conservation, single phase flow equation can be written as,

$$\rho_w S_{\in w} \frac{\partial(p_f)}{\partial t} + \nabla \cdot \rho_w \left[-\frac{k}{\mu_w} \left(\nabla p_f + \rho_w g \nabla h \right) \right] = -\alpha \frac{\partial(\rho_w \varepsilon_{vol})}{\partial t} \tag{2}$$

$S_{\in w}$ is the constrained water fluid storage coefficient which is a function of porosity, φ, Biot coefficient, α, water compressibility, c_w, and drained bulk modulus, K_d, given by,

$$S_{\in w} = \varphi c_w + (\alpha - \varphi) \frac{1 - \alpha}{K_d} \tag{3}$$

Where, $K_d = \frac{2v(1+G)}{3} / (1 - 2v)$

Lastly solid deformation complies with force equilibrium:

$$\nabla \cdot \sigma + (\rho_w \varphi + \rho_d) g = 0 \tag{4}$$

Where, ρ_d denotes dry density of porous medium. For a fully coupled flow, Eqs. (1), (2), and (4) are fully coupled during the fully-implicit numerical simulation, and computation iterates among these equations at each time-step using a finite-element method.

2.2 Governing Equations for Two Phase Flow

In this formulation, we combine the constitutive equation of solid mechanics with the transient formulations of two phase immiscible fluid flow based on Biot's theory (COSMOL 2015; Kim and Hosseini 2017; Jaeger et al. 2007). The constitutive equation of solid mechanics is the same as shown in Eq. 1. From the mass conservation, two-phase immiscible flow equation can be written as,

$$\varphi \frac{\partial(\rho_g S_g)}{\partial t} + \nabla \cdot (\rho_g u_g) = Q_g \tag{5}$$

$$\varphi \frac{\partial(\rho_w S_w)}{\partial t} + \nabla \cdot (\rho_w u_w) = Q_w \tag{6}$$

Assuming each phase's solid-to-fluid coupling effect is linearly proportional to its saturation and density; for a fully coupled flow, the divergence of the displacement for each phase acts as a source term for the flow equations (5) and (6) respectively, given by

$$\varphi \frac{\partial(\rho_g S_g)}{\partial t} + \nabla \cdot (\rho_g u_g) = -\alpha \frac{\partial(\rho_g S_g \varepsilon_{vol})}{\partial t} \tag{7}$$

$$\varphi \frac{\partial(\rho_w S_w)}{\partial t} + \nabla \cdot (\rho_w u_w) = -\alpha \frac{\partial(\rho_w S_w \varepsilon_{vol})}{\partial t} \tag{8}$$

Darcy velocity, u_g and u_w can be written as,

$$u_g = -\lambda_g(\nabla p_g + \rho_g g \nabla h) \tag{9}$$

$$u_w = -\lambda_w(\nabla p_w + \rho_w g \nabla h) \tag{10}$$

where, $\lambda_g = \frac{k_g}{\mu_g}$ and $\lambda_w = \frac{k_w}{\mu_w}$

Storage model can be written as,

$$\varphi \frac{\partial(\rho_g S_g)}{\partial t} = \rho_g S_g S_{\in g} \frac{\partial(p_g)}{\partial t} + \varphi \rho_g \frac{\partial(S_g)}{\partial t} \tag{11}$$

$$\varphi \frac{\partial(\rho_w S_w)}{\partial t} = \rho_w S_w S_{\in w} \frac{\partial(p_w)}{\partial t} + \varphi \rho_w \frac{\partial(S_w)}{\partial t} \tag{12}$$

Where, $S_{\in g}$ is the constrained CO_2 storage coefficient which is a function of porosity, φ, Biot coefficient, α, supercritical CO_2 compressibility, c_g, and drained bulk modulus, K_d, given by (Kim and Hosseini 2013),

$$S_{\in g} = \varphi c_g + (\alpha - \varphi) \frac{1-\alpha}{K_d}$$

And, $S_{\in w}$ is the constrained water storage coefficient, given by Eq. 3.

After simplifying Eq. (7), and substituting Eqs. (9), and (11) in it, Eq. (7) becomes,

$$\rho_g S_g S_{\in g} \frac{\partial(p_g)}{\partial t} + (\varphi \rho_g + \alpha \rho_g \varepsilon_{vol}) \frac{\partial(S_g)}{\partial t} + \nabla \cdot$$
$$\rho_g[-\lambda_g(\nabla p_g + \rho_g g \nabla h)] = -\alpha S_g \frac{\partial(\rho_g \varepsilon_{vol})}{\partial t} \tag{13}$$

CO_2 phase pressure, p_g can be written in term of water pressure, p_w and capillary pressure, p_c, as,

$$p_g = p_w + p_c$$

In terms of p_w and S_g, Eq. 13 can be written as,

$$\rho_g S_g S_{\in g} \frac{\partial(p_w)}{\partial t} + (\varphi \rho_g + \rho_g S_g S_{\in g} \frac{\partial p_c}{\partial S_g} +$$
$$\alpha \rho_g \varepsilon_{vol}) \frac{\partial(S_g)}{\partial t} + \nabla \cdot \rho_g \left[-\lambda_g (\nabla p_w + \frac{\partial p_c}{\partial S_g} \nabla S_g +$$
$$\rho_g g \nabla h) \right] = -\alpha S_g \frac{\partial(\rho_g \varepsilon_{vol})}{\partial t} \tag{13a}$$

Similarly, simplifying Eq. (8) and substituting Eqs. (10) and (12) in it, Eq. (8) becomes,

$$\rho_w S_w S_{\in w} \frac{\partial(p_w)}{\partial t} + (\varphi \rho_w + \alpha \rho_w \varepsilon_{vol}) \frac{\partial(S_w)}{\partial t} + \nabla \cdot$$
$$\rho_w[-\lambda_w(\nabla p_w + \rho_w g \nabla h)] = -\alpha S_w \frac{\partial(\rho_w \varepsilon_{vol})}{\partial t} \tag{14}$$

In terms of p_w and S_g, Eq. 14 can be written as,

$$\rho_w(1 - S_g)S_{\in w} \frac{\partial(p_w)}{\partial t} - (\varphi \rho_w + \alpha \rho_w \varepsilon_{vol}) \frac{\partial(S_g)}{\partial t} + \nabla \cdot$$
$$\rho_w[-\lambda_w(\nabla p_w + \rho_w g \nabla h)] = -\alpha(1 - S_g) \frac{\partial(\rho_w \varepsilon_{vol})}{\partial t}$$
$$\tag{14a}$$

Lastly solid deformation complies with force equilibrium:

$$\nabla \cdot \sigma + \left(\left((1 - S_g)\rho_w + S_g \rho_g \right)\varphi + \rho_d \right) g = 0 \tag{15}$$

Eqs. (1), (13a), (14a) and (15) are fully coupled during the numerical simulation, and computation iterates among these equations at each time-step using a finite-element method.

Overall pore pressure, p_f is given by,

$$p_f = (1 - S_g)p_w + S_g(p_w + p_c) \tag{16}$$

3. Simulation Model and Boundary Conditions

In this study, we consider the three-layer geometry where the permeable sandstone formation is bounded by the basement rocks including faults at the bottom and the thick mud rock at the top as shown in Fig. 1 (Chang and Segall 2016). We impose the fluids

injection at the constant volumetric rate Q=3000 m^3/s (at subsurface condition of initial reservoir pressure=20MPa and temperature=150°F) per unit cross-section area of the reservoir (ms^{-1}) on the left side of the permeable sandstone formation till 30 days. Other reservoir and operating properties are shown in Table 1.
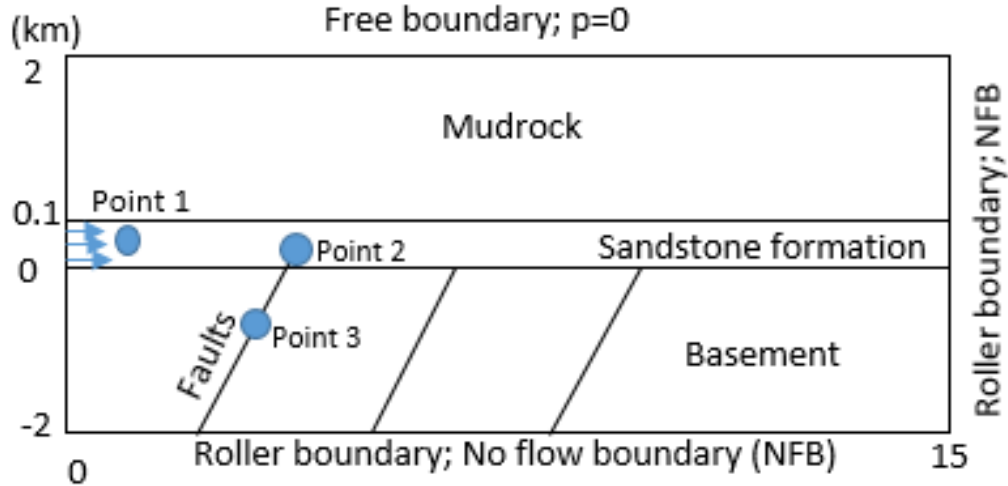

Figure 1 Schematic of three-layer geometry with target formation surrounded by basement rock and mud rock (After Chang and Segall, 2016)

Table 1. Reservoir properties along with operating parameters values

Parameters	Unit	Value
Volumetric injection rate (Q) at the reservoir condition	m^3/s	3000
Length of Target Formation	km	15
Thickness of target formation	m	100
Initial formation pressure	MPa	20
Formation temperature (T)	°F	150
Depth of target formation	m	1,900

The surrounding layers have a low permeability value so they act as a hydraulic barrier. The low permeable mudrock being highly compressible act as a confining unit for fluid injection and lateral pressure propagation. The top, bottom and side boundaries except the fluid inlet act as the no flow boundaries. Mechanically, a roller is imposed on the bottom and side boundaries, so that they are fixed in the normal direction to boundaries but free to move in the parallel direction. The top surface is a free movement surface. The initial conditions for the change in pore pressure and stresses are given by,

$$p_f(x, t = 0) = 0$$

$$\sigma_{xx}(x, t = 0) = \sigma_{zz}(x, t = 0) = \sigma_{yy}(x, t = 0) = 0 ;$$

Initial self-equilibrated change in stresses and pore pressure are set to be zero, so actual pore pressure, P at any time, is equal to,

$$P = 20MPa + p_f$$

Petrophysical and mechanical properties of the sandstone formation and overlying mudrock shown in Table 2 are from the Cranfield field in southwestern Mississippi (Chang and Segall 2016), USA, where one

of the largest CO_2 injection projects has taken place (Kim and Hosseini 2013).

Table 2. Summary of model properties (Chang and Segall, 2016)

Model properties	**Unit**	**Mudrock**	**Sandstone**	**Basement**	**Fault**
Permeability	m^2	10^{-19}	6.4×10^{-14}	2×10^{-17}	10^{-13}
density	kg/m^3	2,600	2,500	2,740	2,500
Shear modulus	GPa	11.5	7.6	25	6
Biot's constant	-	0.35	0.55	0.24	0.79
Poisson's ratio	-	0.3	0.15	0.2	0.2
Porosity	-	0.1	0.25	0.05	0.02
Friction factor, f	-	0.5	0.6	0.6	0.1, 0.75

Relative permeability shown in Table 3 is obtained from Brooks and Corey's (1964) model, while capillary pressure data of immiscible CO_2-water flow shown in Table 3 is obtained from Van-Genutchen's (1980) model.

Table 3 Capillary pressure and relative permeability data

Gas saturation, S_g	Capillary pressure, p_c (Pa)
0	4.7
0.1	55.6
0.2	136.4
0.3	261.5
0.4	480
0.5	885.7
0.6	1904
0.7	6227
0.8	254200

Gas saturation, S_g	Water relative permeability, k_{rw}	Gas relative permeability, k_{rg}
0	1.000	0.000
0.1	0.59	0.0037
0.2	0.316	0.027
0.3	0.152	0.085
0.4	0.0625	0.1875
0.5	0.02	0.336
0.6	0.004	0.527
0.7	0.00025	0.753
0.8	0.000	1.000

Fluid properties including viscosity, density, and compressibility are obtained from the correlations shown in the paper by Mathias et al. 2009. Batzle and Wang (1992) provide the following function for brine density, ρ_w (kgm^{-3}):

$$\rho_w = \rho_W + C\{0.668 + 0.44C + 10^{-6}[300P - 2400PC + T_c(80 + 3T_c - 3300C - 13P + 47PC)]\} \tag{17}$$

Fresh water density, ρ_W, is given by,
$$\rho_W = 1 + 10^{-6}(-80T_c - 3.3T_c^2 + 0.00175T_c^3 + 489P - 2T_cP + 0.016T_c^2P - 1.3 \times 10^{-5}T_c^3P - 0.333P^2 - 0.002T_cP^2 \tag{18}$$

Where, T_c is temperature in ℃, P is pressure in MPa, and C is the solute concentration of sodium chloride in kgl^{-1}. Brine viscosity can be approximated by (Kestin et al. 1981; Batzle and Wang 1992):
$$\mu_w = 0.1 + 0.333C + (1.65 + 91.9C^3)exp\{-[0.42(C^{0.8} - 0.17)^2 + 0.045]T_c^{0.8}\} \tag{19}$$

Where brine viscosity, μ_w is in mPa·s. Brine compressibility is given by (Batzle and Wang 1992);

$$c_w = \frac{1}{\rho_w}\frac{d\rho_w}{dP} = \frac{1}{\rho_w}\left(\frac{d\rho_W}{dP} + C\{10^{-6}[300 - 2400C + T_c(-13 + 47C)]\}\right) \tag{20}$$

$$\frac{d\rho_W}{dP} = 10^{-6}(489 - 2T_c + 0.016T_c^2 - 1.3 \times 10^{-5}T_c^3 - 0.666P - 0.004T_cP) \tag{21}$$

In this study, the high compressibility of supercritical CO_2 has been introduced in the modeling to observe the dissipative effect of CO_2 during the building up of injection induced overpressure. Spycher et al. 2003 used a modified form of the Redlich-Kwong equation of state for supercritical carbon dioxide, given by,

$$P = \left(\frac{RT_k}{V - b_2}\right) - \left(\frac{b_1}{T_k^{0.5}V(V + b_2)}\right) \tag{22}$$

Where, b_1 and b_2 represent measures of intermolecular attraction and repulsion, respectively, V is the molar volume of the compressed gas phase at pressure P (in bars) and temperature T_k (in Kelvin), $R = 83.1447 \, \text{bar} \, cm^3 mol^{-1} K^{-1}$ is the gas constant, $b_1 = 7.54 \times 10^7 - 4.13 \times 10^4 T_k$ and $b_2 = 27.8$. The volume can be obtained by the iterative solution. The density ($kg m^{-3}$) can be obtained as, $\rho_g = 1000 M / V$, where $M = 44.01 \mu g mol^{-1}$ is the molar mass of CO_2. CO_2 viscosity, μ_g is obtained after applying linear regression (Mathias et al. 2009), given by,

$$\mu_g \approx 16.485 + \left(0.0094870\rho_g\right)^2 + \left(0.0025939\rho_g\right)^4 + \left(0.0019815\rho_g\right)^6 \quad (23)$$

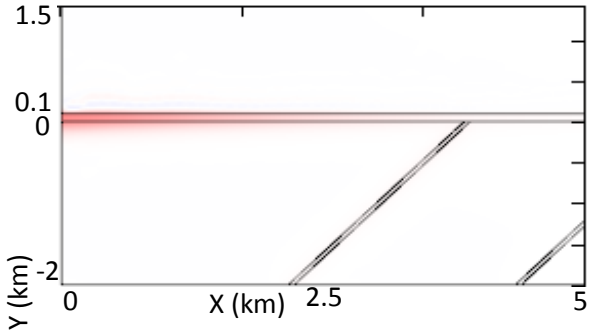Where, μ_g is in $\mu Pa \cdot s$ and ρ_g is in $kg m^{-3}$. The compressibility is obtained from (Bear, 1979):

$$c_g = \frac{1}{\rho_g}\frac{d\rho_g}{dP} = -\frac{1}{V}\frac{dV}{dP} \quad (24)$$

Where, $\frac{dP}{dV} = -\left(\frac{RT_k}{(V-b_2)^2}\right) + \left(\frac{b_1(2V+b_2)}{T_k^{0.5}V^2(V+b_2)^2}\right) \quad (25)$

To investigate the poroelastic response of basement faults to supercritical CO_2 injection and compare with those of water injection, both injected at a constant volumetric rate at subsurface condition, we consider a set of normal faults with dip angle $\theta = 60°$. We compute the normal and shear stresses on faults by assuming only one case of high permeability conduits connected to the target formation, where significant stress changes would occur due to direct pore pressure diffusion in contrast to insignificant change due to indirect poroelastic stressing (Chang and Segall, 2016). We did not consider the case of sealed and isolated faults that are more impacted by indirect poroelastic stressing in this study. We check for any potential of reactivation of preexisting faults via shear slip, which, in most cases, is likely to occur prior to tensile failure.

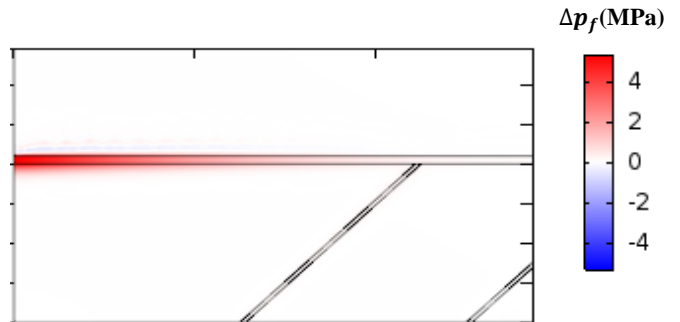## 4. Numerical Results and Analysis

We investigated the two dimensional fields of pore-pressure, normal and shear stresses acting on a plane parallel to the faults at two different time elapses: $t = 30$ days (end of constant injection period), and $t = 150$ days (post injection period) as shown in Figs. 2 to 4. In each figure, left columns show results for the single-phase flow simulation where water is the injecting fluid (slightly compressible), while the right columns show those for the two-phase flow condition considering supercritical CO_2 as the injecting fluid (highly compressible). Here, we will demonstrate any differences, if exists, in the injection-induced stress changes between the two-phase flow and single-phase flow simulation conditions.

Figs 2a and b show the changes in the spatial distribution of pore pressure at the end of 30 days. From figures, we can observe the higher increase in the pore pressure in the two-phase flow condition. It is attributable to the slower pressure diffusion due to lower hydraulic diffusivity of two-phase flow that causes the pore pressure near the injection source to buildup and exceed that of single phase flow as shown in Fig. 3a. Hydraulic diffusivity for two phase flow condition is lower because of a) higher compressibility of supercritical CO_2, and b) effective permeability of fluids in two-phase flow is lower than the absolute permeability considered in single-phase flow. The slower hydraulic diffusion has an impact on the pore pressure buildup at point 2 (refer to Fig. 1), where the pore pressure increment in the two-phase flow is smaller than that in the single-phase flow during certain period of time as demonstrated in Fig. 3b. After this period, diffusion due to higher pore pressure buildup (near the injection-source) in the two-phase flow elevates the pore pressure more than that of single-phase flow (Fig. 3b).

After the end of injection, pore pressure continues to diffuse through the formation, faults and basement as shown in Figs. 2c and d. As a result, higher pore pressure buildup in the two-phase flow condition causes higher pore pressure changes in the basement and faults.
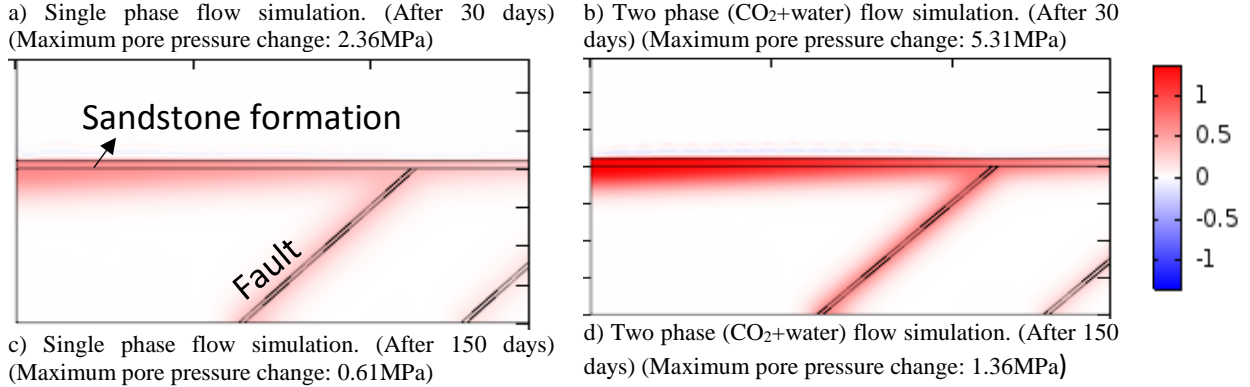
Δp_f(MPa)

a) Single phase flow simulation. (After 30 days) (Maximum pore pressure change: 2.36MPa)

b) Two phase (CO_2+water) flow simulation. (After 30 days) (Maximum pore pressure change: 5.31MPa)

c) Single phase flow simulation. (After 150 days) (Maximum pore pressure change: 0.61MPa)

d) Two phase (CO_2+water) flow simulation. (After 150 days) (Maximum pore pressure change: 1.36MPa)

Figure 2 Comparison of Pore pressure changes, Δp_f(MPa) between the single phase fluid flow and two phase flow conditions from coupled poroelasticity model at t=30, and 150 days for conductive faults
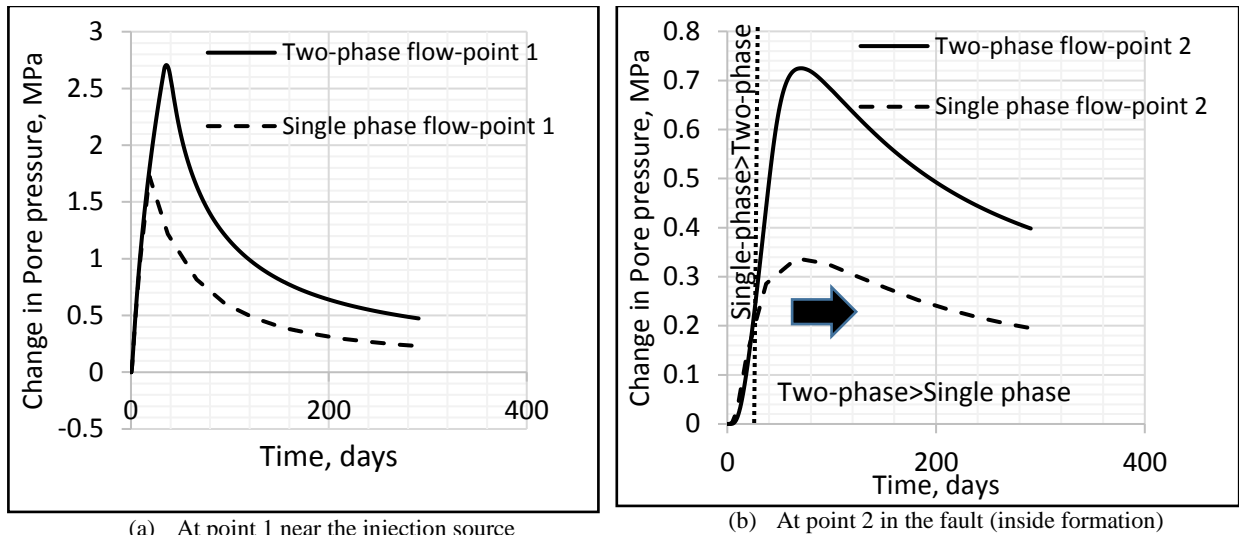

(a) At point 1 near the injection source

(b) At point 2 in the fault (inside formation)

Figure 3 Comparison of change in pore pressure at points 1 and 2 (refer Fig. 1) for single-phase flow and two-phase flow conditions

Figs. 4 show the compressive normal stress changes due to the pore pressure buildup, causing expansion of formation and faults. Compressive stress buildup is higher for the two-phase flow condition as compared to that for the single-phase flow condition. It is because of the higher pore pressure buildup in the two-phase flow condition. We ignore the effect of indirect poroelastic stressing due to pore pressure buildup, as it is insignificant for the given simulation study. Figs. 5 show the shear stress changes in correspondence to fluid flow. As shown in Figs. 5c and d, negative shear

stress develops in the target formation while positive shear stress develops in the faults. This is because the pore pressure buildup inside the faults causes the displacement vectors to change (displacement in the hanging wall changes from lateral to vertical), which results in the positive shear strain and hence, the positive shear stress in the faults. Further, Figs. 5 demonstrate the higher change in the shear stress for the two-phase flow condition as compared to those for the single-phase flow condition, due to the larger change in the pore pressure
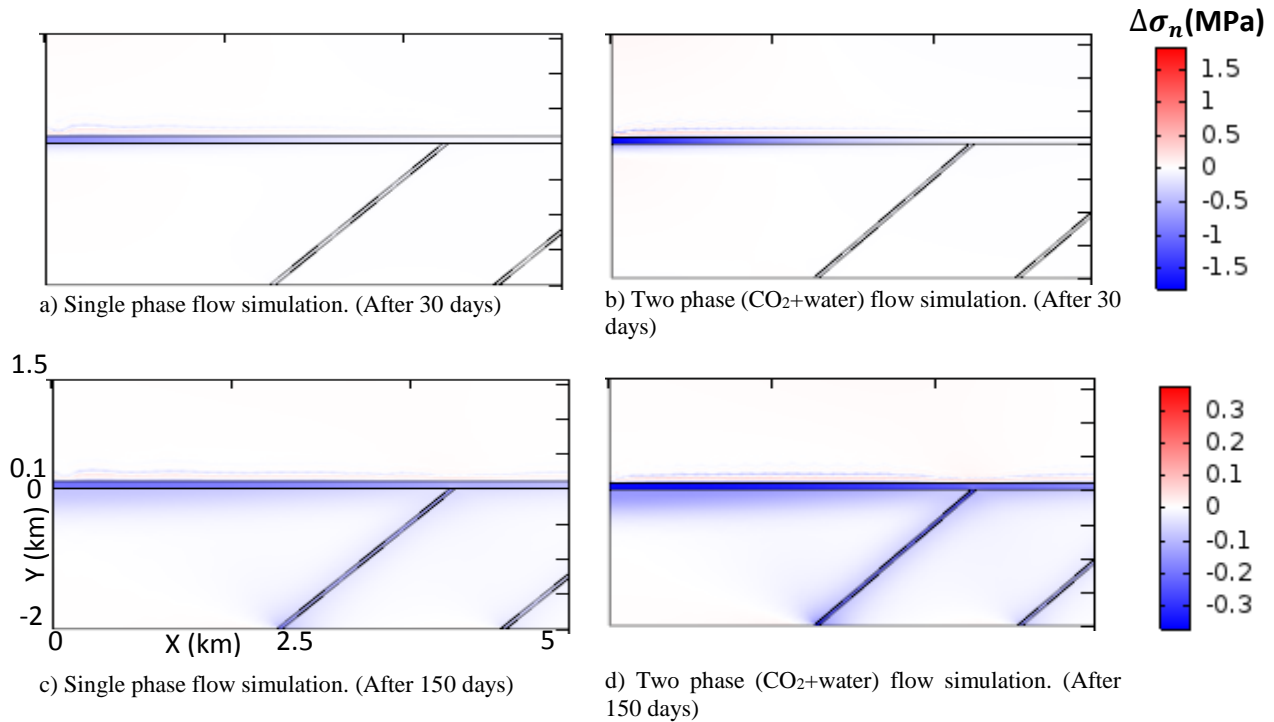
.

a) Single phase flow simulation. (After 30 days)

b) Two phase (CO2+water) flow simulation. (After 30 days)

c) Single phase flow simulation. (After 150 days)

d) Two phase (CO2+water) flow simulation. (After 150 days)

Figure 4 Comparison of Normal stress changes, $\Delta\sigma_n$(MPa) between single-phase flow and two-phase flow condition from coupled poroelasticity model at t=30, and 150 days for conductive faults
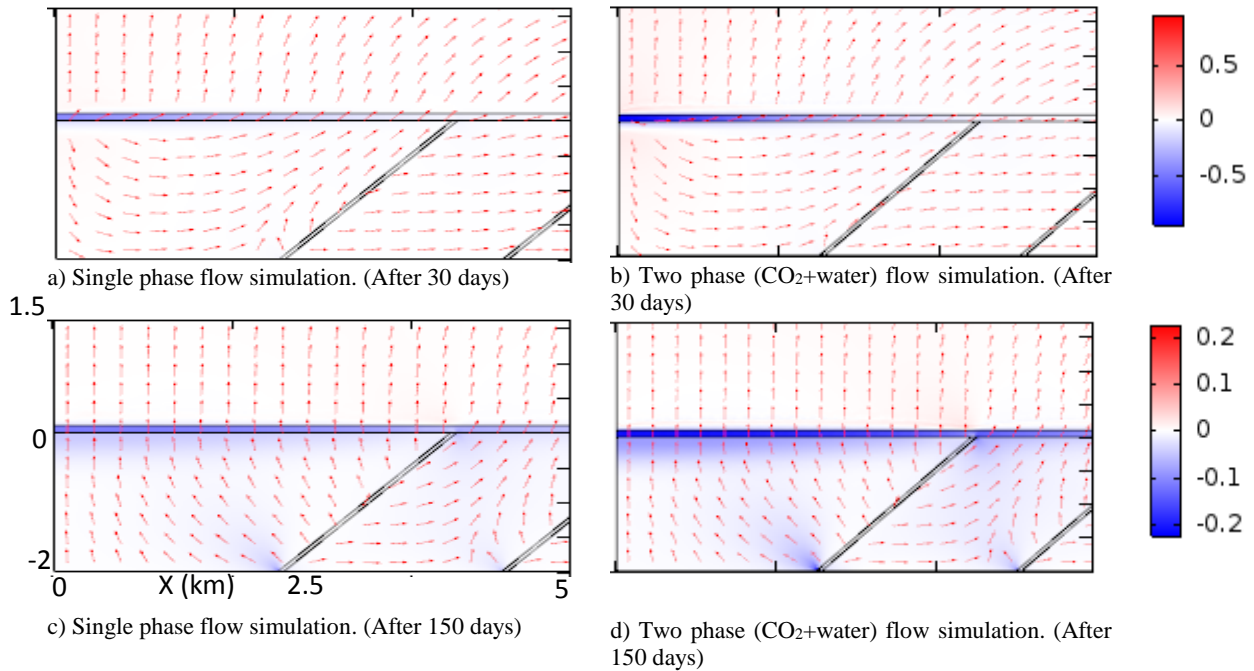

a) Single phase flow simulation. (After 30 days)

b) Two phase (CO2+water) flow simulation. (After 30 days)

c) Single phase flow simulation. (After 150 days)

d) Two phase (CO2+water) flow simulation. (After 150 days)

Figure 5. Comparison of shear stress changes, $\Delta\tau_s$ (MPa) between the single-phase flow and two-phase flow conditions from coupled poroelasticity model at t=30, and 150 days for conductive faults

Assuming the friction coefficient 'f' remains constant, the change in coulomb stress on a failure plane can be defined as follows,

$$\Delta\tau = \Delta\tau_s + f(\Delta\sigma_n + \Delta p_f) \qquad (26)$$

Fig. 7a shows the evolution of pore pressure changes with time at two different points 2 and 3 (refer to Fig.

9

1) for the two-phase flow simulation condition. The plots reveal that the change in pore pressure increases initially due to the propagation of overpressure front from the injection well, and thereafter decreases due to the gradual diffusion of excess pore pressure to surrounding layers as the pressure front expands into these areas. Faults also acts as a virtual source of lateral pressure diffusion into the basement rock. Fig. 7b shows that the coulomb stress increase at point 2 is higher than that at point 1 because of two reasons: a) more compressive normal stress develops in the basement as compared to the fault (Figs. 4c and d); b) positive shear stress is induced in the fault, whereas the change is negative in the target formation (Figs. 5c and d). Moreover, the pattern of coulomb stress changes shown in Figs. 6 and Fig. 7b resembles that of pore pressure changes (Figs. 2 and Fig. 7a, respectively). It implies that the stress evolution of basement fault is predominantly affected by the pore

pressure resulting from direct diffusion of it. And because the pore pressure increase in the faults are higher for the two-phase fluid flow condition, we can observe the greater increase of coulomb stress as well (Figs. 6 and Figs. 8b), which translates a higher chance of fault slippage failure. Discrepancy in the change of coulomb stress between single- and two-phase flow condition can be as twice large (Figure 8b), which suggests that employing the single-phase fluid flow condition may significantly underestimate the likelihood of slip-induced failure or injection-induced seismicity along the faults in the basement layers. Note that even though trivial increase of coulomb stress was observed beyond the direct impact of elevated pore pressure for both flow conditions (Figs. 6a and b), indirect poroelastic stressing may become significant at higher injection rate. This aspect will be examined in the following study.
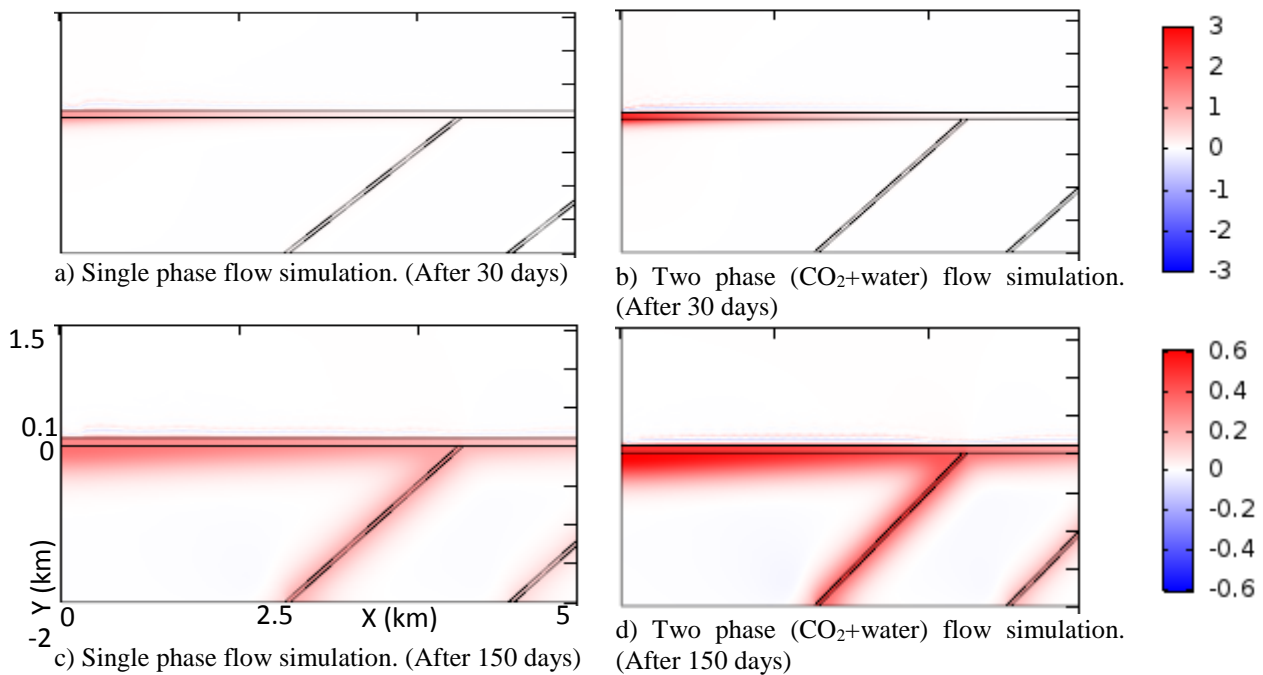

a) Single phase flow simulation. (After 30 days)

b) Two phase (CO_2+water) flow simulation. (After 30 days)

c) Single phase flow simulation. (After 150 days)

d) Two phase (CO_2+water) flow simulation. (After 150 days)

Figure 6. Comparison of change in coulomb stress between single-phase and two-phase fluid flow condition due to poroelastic stressing, $\Delta\tau$ (MPa) at t=30, and 150 days for conductive faults
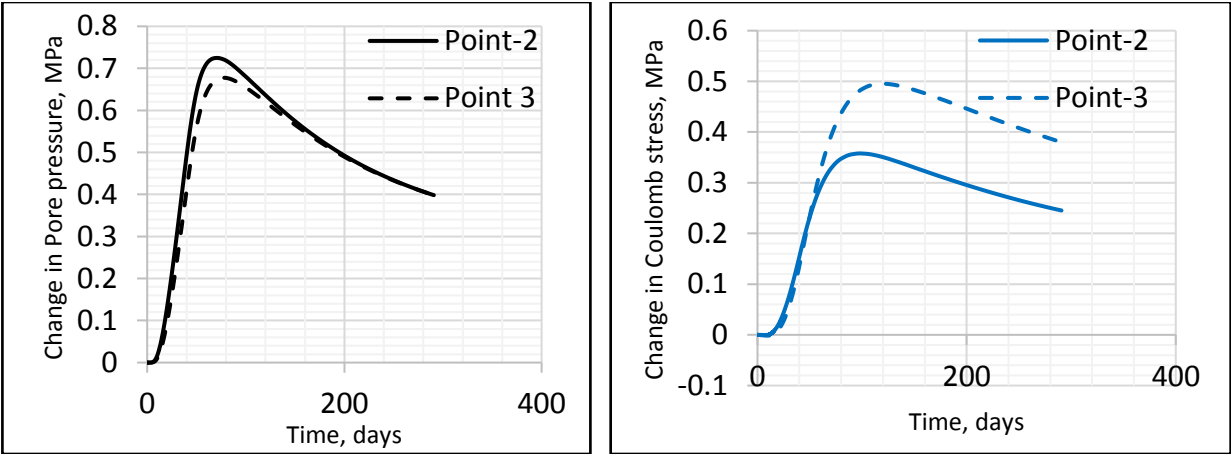
(a) Change in pore pressure vs. time (b) Change in coulomb stress vs. time

Figure 7. Change in pore pressure (a) and coulomb stress (b) vs. time at points 1 (in formation) and 2 (in fault) (refer to Fig. 1) for two-phase (CO_2+water) flow condition
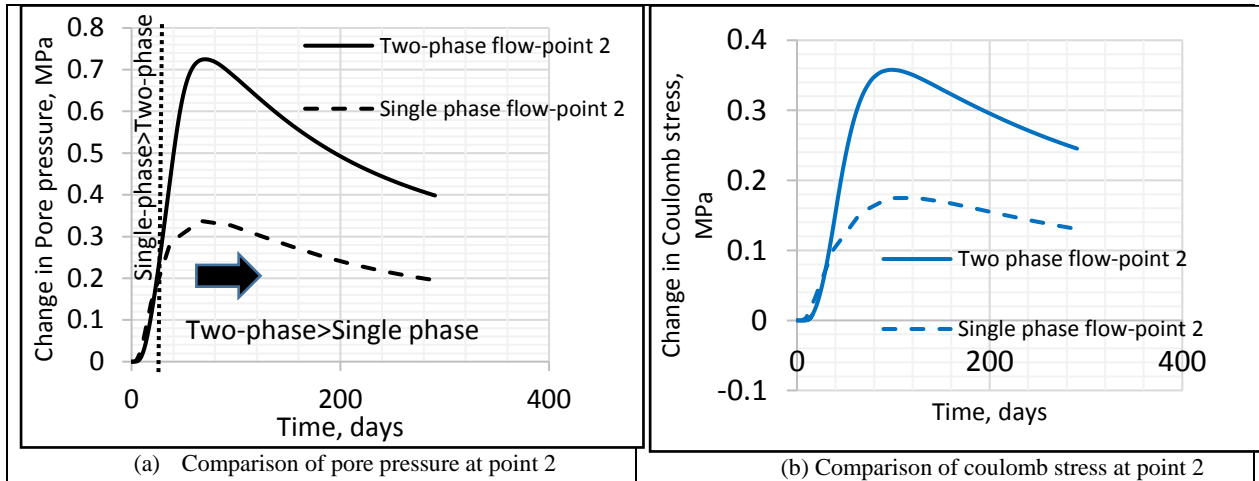
(a) Comparison of pore pressure at point 2 (b) Comparison of coulomb stress at point 2

Figure 8. Comparison of pore pressure and coulomb stress at point 2 (refer to Fig. 1) between the single-phase and two-phase fluid flow conditions

5. Conclusions

Salient observations of this study are as follows:

1.) Transient formulations of single-phase fluid flow and two-phase immiscible fluid flow are developed and combined with the constitutive equation of solid mechanics based on Biot's theory using the equation based modeling interface in COMSOL. Gravity and capillary effects are incorporated, but the partial miscibility of CO_2 and water is not considered in the derivation. After that, numerical simulation results of the two-phase flow of supercritical CO_2 and water is compared with those of the single-phase (water) flow condition.

2.) In a layered-structure, injection-induced pore pressure dissipates into the basement and conductive faults, which leads to changes in the stress state. Employment of two-phase flow simulation of CO_2 and water predicts higher pore pressure buildup in the target storage formation and in faults as compared to that of single-phase flow simulation. It is because higher pressure buildup is induced near the injection well as a result of lower hydraulic diffusivity in the two-phase flow condition and thus slower pressure diffusion.

3.) Lower pressure buildup in the single-phase fluid flow condition underestimates the change of normal and shear stresses in the

11

target formation and conductive faults where direct pore pressure propagation prevails.

4.) Consequently, it may lead to the underestimate of the coulomb stress increase in the target formation and faults in the basement. This implies that the single-phase fluid flow condition can potentially underestimate the injection-induced seismicity particularly when conductive faults are under the direct influence of pore pressure propagation from the target formation.

5.) Increase in the coulomb stress is higher on the fault in the basement than in the target storage formation. It suggests that a chance of failure or potential seismicity is greater in the basement.

Nomenclature

σ = stress

C = elasticity matrix

ε = strain

α = biot's constant

I = identity matrix

p_f = pore pressure

φ = porosity

ρ_g = density of CO2, kgm^{-3}

S_g = CO2 saturation

u_g = velocity of CO2, m/s

Q = Volumetric rate at reservoir conditions, m^3/s

ρ_w = density of water, kgm^{-3}

S_w = Water saturation

u_w = velocity of water, m/s

ε_{vol} = volumetric strain

λ_g = mobility of gas, $m^2/Pa.s$

λ_w = mobility of water, $m^2/Pa.s$

$S_{\in g}$ = constrained CO2 phase storage coefficient, Pa^{-1}

$S_{\in w}$ = constrained water phase storage coefficient, Pa^{-1}

c_g = compressibility of CO2 phase, Pa^{-1}

c_w = brine (water phase) compressibility, Pa^{-1}

K_d = drained bulk modulus, Pa

k_g = effective permeability of CO2, m^2

μ_g = viscosity of CO2, Pa.s

k_w = effective permeability of water, m^2

p_g = CO2 phase pressure, Pa

p_w = water phase pressure, Pa

p_c = capillary pressure, Pa

σ_{xx} = normal stress in X-direction, Pa

σ_{yy} = normal stress in Y-direction, Pa

σ_{zz} = normal stress in Z-direction, Pa

ρ_W = fresh water density, kgm^{-3}

ρ_w = brine water density, kgm^{-3}

T_c = temperature, °C,

P = pressure, MPa

C = solute concentration of sodium chloride, kgl^{-1}

μ_w = brine viscosity, mPas

V = molar volume of the compressed gas phase, cm^{-3}

T_k = temperature, Kelvin

M = molar mass of CO2, $\mu gmol^{-1}$

τ_s = shear stress, MPa

τ = coulomb stress, MPa

σ_n = normal stress, MPa

f = friction coefficient

k = absolute permeability of the medium, m^2

References

1. Horton, S., Disposal of Hydrofracking Waste Water Fluid by Injection into Subsurface Aquifer Triggers Earthquake Swarm in Central Arkansas with Potential for Damaging Earthquake. *Seismol. Res. Lett*., 83(2), 250-260 (2012).

2. Kim, W.Y., Induced Seismicity Associated With Fluid Injection Into a Deep Well in Youngstown, Ohio. *J. Geophys. Res. Solid Earth,* 118, 3506-3518 (2013).

3. Ellsworth, W.L., Injection-Induced Earthquakes. *Science*, 341 (6142), 1225942 (2013).

4. Kerenan, K.M., Savage, H.M., Abers, G.A., and Cochran, E.S., Potentially Induced Earthquakes in Oklahoma, USA: Links between Wastewater Injection and the 2011 M_w 5.7 Earthquake Sequence. *Geology*, 41, 699-702 (2013).

5. Zoback M.D., The potential for triggered seismicity associated with geologic sequestration of CO2 in saline aquifers. *American Geophysical Union (AGU), EOS Trans. AGU*, 91(52), Fall Meeting, Suppl., Abstract NH11C-01 (2010).

6. Bauer, R.A., Carney, M., and Finley, R.J., Overview of Microseismic Response to CO2 Injection into the Mt. Simon Saline Reservoir at the Illinois Basin-Decatur Project. *International Journal of Greenhouse Gas Control*, 54 (1), 378-388 (2016).

7. Haring, M.O., Schanz U., Ladner F., Dyer B.C., Characterisation of the basel 1 enhanced geothermal system. *Geothermics* 37, 469–495 (2008).

8. Chiaramonte, L., Zoback, M. D., Friedmann, J., & Stamp, V., Seal integrity and feasibility of CO 2 sequestration in the Teapot Dome EOR pilot: geomechanical site characterization. *Environmental Geology*, *54*(8), 1667-1675 (2008).

9. Hillis, R., Pore pressure/stress coupling and its implications for seismicity. *Exploration Geophysics*, *31*(1/2), 448-454 (2000).

10. Hillis, R. R., Coupled changes in pore pressure and stress in oil fields and sedimentary basins. *Petroleum Geoscience*, *7*(4), 419-425 (2001).

11. Kim, S. and Hosseini, S., Above-Zone Pressure Monitoring and Geomechanical Analyses for a Field-Scale CO2 Injection Project, Cranfield, MS. *Greenhouse Gases Sci. Technol*., 4, 81-98 (2013).

12. Kim. S., and Hosseini, S., Geological CO2 Storage: Incorporation of Pore-Pressure/Stress Coupling and Thermal Effects to Determine Maximum Sustainable Pressure Limit. Energy Procedia 63, 3563-3567 (2014).

13. Kim. S., and Hosseini, S., Hydro-thermo-Mechanical Analysis During Injection of Cold Fluid into a Geologic Formation. Int. J. Rock Mech. Min. Sci. 77, 220-236 (2015).

14. Kim. S., and Hosseini, S., Study on the Ratio of Pore-Pressure/Stress Changes During Fluid Injection and its Implications for CO2 Geologic Storage. *Journal of Petroleum Science and Engineering*, 149, 138-150 (2017).

15. Rutqvist J., Wu Y.S., Tsang C.F., Bodvarsson G.A., Modeling approach for analysis of coupled multiphase fluid flow, heat transfer, and deformation in fractured porous rock. *Int J Rock Mech Min Sci* 39, 429–442 (2002).

16. Rutqvist J., Status of the TOUGH-FLAC simulator and recent applications related to coupled fluid flow and crustal deformations. *Comput Geosci*, 37, 739–750 (2011).

17. Bower, K. M., & Zyvoloski, G., A numerical model for thermo-hydro-mechanical coupling in fractured rock. *International Journal of Rock Mechanics and Mining Sciences*, *34*(8), 1201-1211 (1997).

18. Deng, H., Dai, Z., Jiao, Z., Stauffer, P. H., & Surdam, R. C., *Simulation of CO2 sequestration at Rock Spring uplift, Wyoming: heterogeneity and uncertainties in storage capacity, injectivity and leakage* (No. LA-UR-11-10385). Los Alamos National Lab.(LANL), Los Alamos, NM (United States) (2011).

19. Olivella, S., Carrera, J., Gens, A., & Alonso, E. E., Nonisothermal multiphase flow of brine and gas through saline media. *Transport in porous media*, *15*(3), 271-293 (1994).

20. Vilarrasa, V., Bolster, D., Olivella, S., & Carrera, J., Coupled hydromechanical modeling of CO2 sequestration in deep saline aquifers. *International Journal of Greenhouse Gas Control*, *4*(6), 910-919 (2010).

21. Ouellet, A., Bérard, T., Desroches, J., Frykman, P., Welsh, P., Minton, J. & Schmidt-Hattenberger, C.,

Reservoir geomechanics for assessing containment in CO_2 storage: a case study at Ketzin, Germany. *Energy Procedia*, *4*, 3298-3305 (2011).

22. CMG, User's guide STARS. Computer Modelling Group Ltd., Calgary (2015).

23. Bissell, R. C., Vasco, D. W., Atbi, M., Hamdani, M., Okwelegbe, M., & Goldwater, M. H., A full field simulation of the in Salah gas production and CO_2 storage project using a coupled geo-mechanical and thermal fluid flow simulator. *Energy Procedia*, *4*, 3290-3297 (2011).

24. Preisig, M., & Prévost, J. H., Coupled multi-phase thermo-poromechanical effects. Case study: CO_2 injection at In Salah, Algeria. *International Journal of Greenhouse Gas Control*, *5*(4), 1055-1064 (2011).

25. Pan, F., Sepehrnoori, K., & Chin, L., Development of a coupled geomechanics model for a parallel compositional reservoir simulator. In *SPE Annual Technical Conference and Exhibition*. Society of Petroleum Engineers (2007).

26. Haddad, M., & Sepehrnoori, K., Development and validation of an explicitly coupled geomechanics module for a compositional reservoir simulator. *Journal of Petroleum Science and Engineering*, *149*, 281-291 (2017).

27. Chin, L. Y., Thomas, L. K., Sylte, J. E., & Pierson, R. G., Iterative coupled analysis of geomechanics and fluid flow for rock compaction in reservoir simulation. *Oil & Gas Science and Technology*, *57*(5), 485-497 (2002).

28. Rohmer, J., & Seyedi, D. M., Coupled large scale hydromechanical modelling for caprock failure risk assessment of CO_2 storage in deep saline aquifers. *Oil & Gas Science and Technology–Revue de l'Institut Français du Pétrole*, *65*(3), 503-517 (2010).

29. Ferronato, M., Gambolati, G., Janna, C., & Teatini, P., Geomechanical issues of anthropogenic CO_2 sequestration in exploited gas fields. *Energy Conversion and Management*, *51*(10), 1918-1928 (2010).

30. Lucier, A., Zoback, M., Gupta, N., & Ramakrishnan, T. S., Geomechanical aspects of CO_2 sequestration in a deep saline reservoir in the Ohio River Valley region. *Environmental Geosciences*, *13*(2), 85-103 (2006).

31. Vidal-Gilbert, S., Tenthorey, E., Dewhurst, D., Ennis-King, J., Van Ruth, P., & Hillis, R., Geomechanical analysis of the Naylor Field, Otway Basin, Australia: Implications for CO_2 injection and storage. *International Journal of Greenhouse Gas Control*, *4*(5), 827-839 (2010).

32. COMSOL, 4.3 User's Guide. COMSOL Multiphysics (2015).

33. Chang, K. W., & Segall, P., Injection-induced seismicity on basement faults including poroelastic stressing. *Journal of Geophysical Research: Solid Earth*, *121*(4), 2708-2726 (2016).

34. Jaeger, J. C., Cook, N. G., & Zimmerman, R., *Fundamentals of rock mechanics*. John Wiley & Sons (2007).

35. Brooks, R., & Corey, T., HYDRAU uc properties of porous media. *Hydrology Papers, Colorado State University*, *24*, 37 (1964).

36. Van Genuchten, M. T., A closed-form equation for predicting the hydraulic conductivity of unsaturated soils 1. *Soil science society of America journal*, *44*(5), 892-898 (1980).

37. Mathias, S. A., Hardisty, P. E., Trudell, M. R., & Zimmerman, R. W. (2009). Approximate solutions for pressure buildup during CO 2 injection in brine aquifers. *Transport in Porous Media*, *79*(2), 265.

38. Batzle, M., & Wang, Z., Seismic properties of pore fluids. *Geophysics*, *57*(11), 1396-1408 (1992).

39. Kestin, J., Khalifa, H. E., & Correia, R. J., Tables of the dynamic and kinematic viscosity of aqueous NaCl solutions in the temperature range 20–150 C and the pressure range 0.1–35 MPa. *Journal of physical and chemical reference data*, *10*(1), 71-88 (1981).

40. Spycher, N., Pruess, K., & Ennis-King, J., CO_2-H2O mixtures in the geological sequestration of CO_2. I. Assessment and calculation of mutual solubilities from 12 to 100 C and up to 600 bar. *Geochimica et cosmochimica acta*, *67*(16), 3015-3031 (2003).

41. Bear, J., *Hydraulics of groundwater*. Courier Corporation (2012).

42. Chiaramonte L., White J.A., Johnson S., Preliminary geomechanical analysis of CO_2 injection at Snøhvit, Norway. In: Proceedings of 45th US Rock mechanics/geomechanics symposium, San Francisco, CA, June 26–29 (2011).